ELSEVIER

Contents lists available at ScienceDirect

Composites Part A

journal homepage: www.elsevier.com/locate/compositesa





Effects of debulking on the fiber microstructure and void distribution in carbon fiber reinforced plastics

Mathew Schey^{a,*}, Tibor Beke^a, Kyle Owens^b, Andy George^b, Evan Pineda^c, Scott Stapleton^a

- ^a Universtiy of Massachusetts Lowell, Lowell, MA 01854, USA
- ^b Brigham Young University, Provo, UT 84602, United States
- ^c NASA Glenn Research Center, Cleveland, OH 44135, United States

ARTICLE INFO

Keywords: Carbon fiber Voids Clusters Debulking

ABSTRACT

Carbon Fiber Reinforced Plastics (CFRPs) are widely used due to their high stiffness to weight ratios. A common process manufacturers use to increase the strength to weight ratio is debulking. Debulking is the process of compacting a dry fibrous reinforcement prior to resin infusion. This process is meant to decrease the average inter-fiber distance, effectively increasing the fiber volume fraction of the sample. While this process is widely understood macroscopically its effects on fibrous microstructures have not yet been well characterized. The aim of this work is to compare the microstructures of three CFRP laminates, varying only the debulking step in the manufacturing process. High resolution serial sections of all three laminates were taken for analysis. Using these scans, the fiber positions were reconstructed. Statistical descriptors such as local fiber and void volume fractions, fiber orientation, and void distribution and morphology were then generated for each sample. Fiber clusters present within the material were identified and analyzed for each level of debulking applied. Using these descriptors, the effects of debulking on the morphology and organization of the composite microstructure was evaluated.

1. Introduction

Carbon Fiber Reinforced Plastics (CFRPs) are widely used as a high-performance material due to their high strength to weight ratios. Traditionally, such CFRPs are manufactured with a carbon fiber textile reinforcement, pre-impregnated with matrix resin (i.e., "prepreg"). To reduce costs, the industry has been moving towards molding with dry reinforcements using a family of processes known as Liquid Composite Molding (LCM). Compared to prepreg materials, working with dry reinforcements incurs fewer material costs, less material waste from both trim and expiration, less freezer storage energy, and more flexibility with complex part geometries. In LCM, the dry reinforcement is laid on the tool, and the fibers are subsequently wet-out with the resin, either by over-pressure in Resin Transfer Molding (RTM) or vacuum draw in Vacuum Infusion (VI). VI is more cost effective for larger parts as the mold consists of one-sided tooling, only rigid enough to support vacuum pressure, and a vacuum bag covering the other side of the reinforcement

Due to the use of a flexible vacuum bag, the driving force for the resin

infusion of the fibers in VI is limited to vacuum pressure only, whereas wet-out in RTM may be performed at whatever pressure the equipment is capable of. The ability to consolidate the CFRP is limited as vacuum pressure by itself will result in a higher porosity and thus more resin content, compared to applying over-pressure to the bag in an autoclave cure, or the high pressures usually involved in RTM. This in turn limits the achievable fiber volume fraction which can be directly tied to the part's mechanical performance. The lower pressures involved in VI can also result in higher void content. Air bubbles trapped in the part after resin cure are then known as voids and act as a further detriment to mechanical performance [2-7]. In comparison with prepreg, all forms of LCM processing also suffer from a less homogeneous distribution of voids due to the in-plane pressure gradient applied during resin wet-out [8–10]. Some prepreg materials, specifically unidirectional tapes, will have less of a tow structure, and thus less of the capillary-viscous flow differences exhibited by textile reinforcements [11], thus further promoting void microstructural homogeneity.

A common process manufacturers use to mitigate the thickness gradient and low fiber content in VI is debulking. In the context of LCM

E-mail addresses: Mathew_Schey@student.uml.edu (M. Schey), Tibor_Beke@uml.edu (T. Beke), Andy_George@byu.edu (A. George), Evan.j.pineda@nasa.gov (E. Pineda), Scott Stapleton@uml.edu (S. Stapleton).

^{*} Corresponding author.

processing, debulking is the process of compacting a dry fibrous reinforcement, via cyclic loading, prior to infusion to induce fiber nesting. The term "debulking" is also used with prepreg materials, where compaction is used not as much to induce fiber nesting but to squeeze out excess resin. In the context of LCM i.e. debulking of dry reinforcements, a hysteresis is seen through repetition of the compaction, where the reinforcement moves to a more nested and compressed state [12–17]. Upon VI processing of such a debulked reinforcement, the same vacuum application and ambient pressure will result in a higher fiber volume fraction than without the debulking [17]. In addition, a debulked reinforcement exhibits less compliance, and thus less of a thickness gradient along the resin flow path [17].

The literature on debulking has focused on experimental determination of the changes in required material thickness to reach a target pressure, or vice-versa, while iterating parameters such as compaction rate, ply count, and reinforcement material [12–17]. Such studies have shown that 1) higher compaction rate causes less compliance [14,15], 2) varying the ply count causes a significant difference in compressibility for only very low ply counts [16], and 3) the increase in nesting between cycles decreases with each subsequent cycle [12,13,15,17,18]. Similar reinforcement compaction studies have focused on the compressibility of the reinforcement during VI processing [19–22], without examining the effects of pre-infusion debulking.

One common observation on both micro-CT scans and serial sections of CFRPs is the presence of voids. Voids appear as extremely dark regions that lay in between individual fibers as well as in between other fibrous structures such as tows and plies. During LCM processing including VI, small amounts of gas are mechanically trapped as bubbles due to the dual scale flow including flow between the fiber tows, and flow within the fiber tows [23-25]. The trapped gas comes from either the resin itself, or from lingering atmospheric gas amid the fibers. Intertow macro-voids are formed when the flow front velocity is low and the intra-tow capillary flow outpaces the inter-tow bulk flow [23]. Intra-tow micro-voids may be formed in the opposite case when the flow front velocity is high and outpaces capillary flow [26,27]. Although debulking may result in enhanced mechanics, it comes at the cost of processability. Greater debulking causes an increase in the fiber volume content, and thus slower filling velocities. As per the dual scale void formation theory outlined above, this should result in more formation of macro-bubbles, i. e., those formed between the tows. With the tighter fiber packing, this will also result in less ability for the trapped bubbles to be flushed to the flow front and out of the resin [28], thus increasing the final void content. No previous studies have investigated this trade-off, namely, how much of an increase in filling time and void content result from a particular amount of debulking.

The effects of debulking on the organization of fibrous microstructures have not yet been well characterized. The one known study on this subject showed a lateral spreading of the fiber tows during the first compaction cycle, leading to a significant rise in the maximum fiber volume fraction and a dependence on the frictional characteristics of the fiber contacts for later cycles [13]. This difference in mechanisms between the first compaction and later ones suggests that the models developed for the compaction occurring during VI processing, based on no debulking [21], cannot accurately predict the behavior of a debulked reinforcement. While the microstructural mechanisms of reinforcement compaction have thus been studied for low cycle counts, only more empirical results have been presented for true debulking practice involving several cycles. Industrial debulking practice is typically developed in a trial-and-error process by individual companies or even individual operators, and usually involves many cycles. This study aims to investigate the actual microstructural mechanism that leads to increased compaction during several cycles of debulking, to enable a better understanding of what process parameters lead to the fastest and most effective debulking practice.

[26] One of the many aspects of CFRPs that has been studied is entanglement. Entanglement is a phenomenon that occurs when fibers

cross over and nest inside one each other. While numerous methods exist for quantifying the entanglement of fiber reinforced composites, little is known about the actual effect of debulking on the entanglement within a microstructure [29–35]. One of the methods for studying entanglement is looking at micrographs of unidirectional CFRPs at sub-micron resolution [31]. Using these images, fiber paths can be reconstructed, and various measurements can be made.

Fast et al., observed that the microstructure underwent deformation that was potentially indicative of the loads the composite was subjected to during manufacturing [26]. One of the major conjectures in this paper was that the final formation of a fiber bundle, from manufacturing, was likely to influence the distribution of resin during infusion and, consequently, the distribution of cracks during failure. This led to the question of whether studying the microstructure itself could provide any information on how the composite was manufactured. The question remains whether the effects of a single manufacturing step could be seen by observing the microstructure using a series of metrics. These include spatial measurements such as local fiber volume fraction and unique neighbor change rate, as well as measurements of the orientation of the fiber with respect to the axial direction. Additionally, observations of key features such fiber cluster can be made. Fiber metrics can also be studied inside these clusters, to get a sense for how clustered fibers behave. Numerous works have been done with the goal of understanding the microstructures using a series of metrics [36,37]. However, the current state of the art has not fully linked the manufacturing process used to create a composite to the resulting organization of the microstructure.

The aim of this work is to compare the microstructures of three CFRP laminates, varying only the debulking step in the manufacturing process. High resolution serial sections of all three laminates were taken using the UES ROBO-MET at the NASA Glenn Research Center in Cleveland, Ohio [38]. Using these scans, the fiber positions were measured and connected to make fiber paths. Statistical descriptors such as local fiber volume fraction, unique neighbor change rate, and void volume fraction and void distribution and morphology, were then generated for each sample and compared. Fiber clusters were also detected in each of the three laminates and analyzed by measuring aspects of their shape and distribution. Additionally, a study on the presence and characteristics of voids was also performed. Using these descriptors, the effects of debulking on the composite microstructure can be measured.

2. Method

Three four-ply stacks of unidirectional dry carbon fiber textile were prepared, with each ply cut to a 254 mm \times 254 mm square. The reinforcement used for all samples was a 24 K fiber/tow carbon unidirectional weave. This weave has an areal weight of 756 g/m² and fiber density of 1770 kg/m³. The resin used was RIMR-135 epoxy resin with RIMH-1366 curing agent. Two of these ply-stacks were subjected to three different levels of debulking before infusion. The third ply-stack was not subjected to any pre-infusion debulking. During the debulking procedure various measurements, such as thickness and pressure, were made and recorded. The ply stacks were each infused separately with resin and cured, and then samples were taken from all three laminates and prepared for imaging. After imaging, the scans were analyzed and fiber paths, void locations and statistics were measured. Metrics describing the density distribution, clustering, and orientation for both the fibers and voids were then generated.

2.1. Debulking and compressibility testing

Various amounts of debulking were performed by compressing the dry reinforcement samples in a universal testing machine (UTM), between flat metal surfaces, at different cycle counts, displacement rates, and durations of compression ("dwell times"). The debulking could also

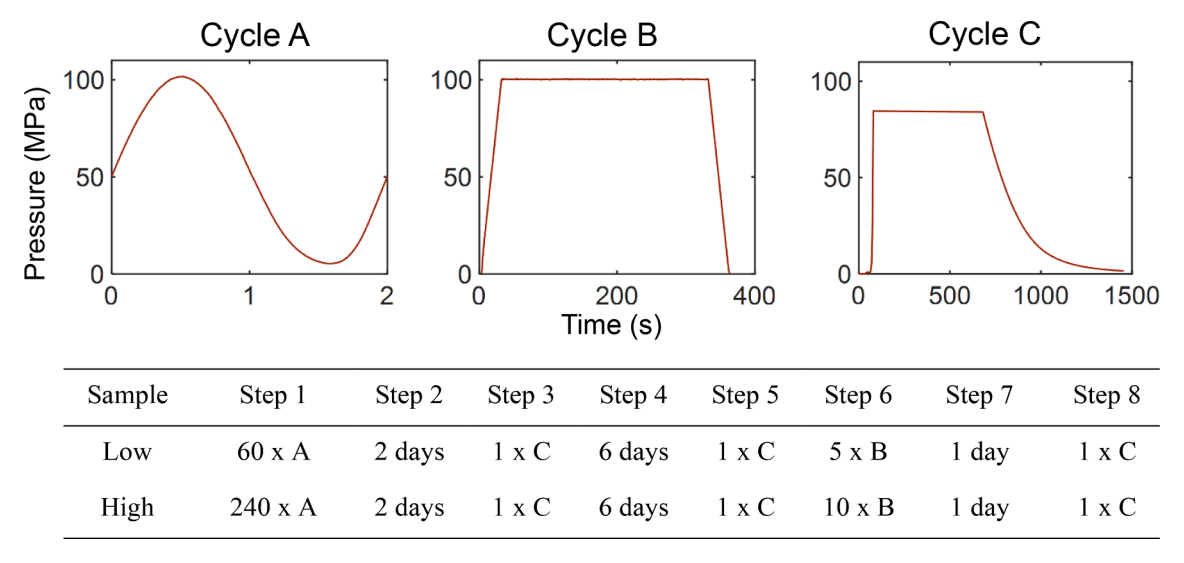


Fig. 1. Diagrams of the three basic debulking cycle types with a table of the applications of each process for both the Low and High debulk samples.

Table 1Breakdown of polishing steps for serial sectioning procedure, including the pad and solution combinations used at each step.

Pad/ Cloth	Solution	Time (s)	Swap Speed (°/S)	Rotation Speed (°/S)
Largo	6μ m Diamond	180	60	30
DAC	3μ m Diamond	180	60	30
DAC	1μ m Diamond	180	60	30
MD-	Colloidal	180	60	30
Chem	Silica			

be performed under a vacuum bag, but UTM is more commonly used in debulking studies [11–15,17] due to the greater control and repeatability. The compressibility of a reinforcement has been shown to be nearly identical for a UTM-pressed dry reinforcement and the same undergoing VI processing [18].

The thickness of the samples and applied pressure were measured over the entire debulking process. All thicknesses were measured from the machine extension and corrected for machine flexibility from similar testing with no sample. From the thickness measurements the volume fraction of the sample was calculated. It was observed that the thickness of the fibers would decrease with debulking steps and then relax back to a fraction of the original thickness. The pressure versus thickness results are shown in the appendix. The pressure versus thickness results are shown in the appendix.

Three different debulking cycle types were performed (Fig. 1):

- 1) Cycle A: 100 kPa pressure applied in 2 s periods.
- 2) Cycle B: 3.5 kPa/s compression to 100 kPa, five minute dwell, and 3.5 kPa relaxation over a total of 6 min.
- Cycle C: 4 mm/min compression to 86 kPa, 15 min dwell, and 0.04 mm/minute relaxation of a 25 min period.

The sequence of debulking for each of the samples is summarized in Fig. 1. The sequence of debulking steps did not change for both samples, while the number of cycles per step did vary at steps 1 and 6. The fibers that underwent the most cycles of debulking per step were deemed the "High" debulking sample, while the other fibers were deemed the "low" debulking. All sample handling was done with care to minimize fabric shear or anything else that could influence the microstructure between the debulking steps.

2.2. Sample preparation and imaging

Three laminates were manufactured by vacuum infusion under a vacuum bag, using a layer of flow media over the top to accelerate the filling time. Two of the laminates were prepared from the "low debulk" and "high debulk" samples from the debulking experiments, which were infused shortly after the last debulking cycle. The third laminate was prepared from a ply-stack straight from the fabric roll, with no debulking, referred to as the "benchmark" sample. Details of the resin infusion process can be found in the appendix. Rectangular 3 mm \times 20 mm \times 50 mm samples were cut from each of the three cured laminates using a wet diamond-tipped saw. Samples were cut from the resin inlet corner of each plate, after the edges of the plates had been squared off. The samples were sanded to remove the peel ply texture from the bagside of the laminate and to a consistent, uniform thickness of 2.8 mm. The peel ply was removed so that the images would consist entirely of fibers.

Serial sections were taken using the UES Robo-Met.3D machine at the NASA Glenn Research Center in Cleveland, Ohio. All three samples were stacked on top of each other and potted in resin as a single sample. The unified sample was placed in the Robo-Met for polishing and imaging. The serial sectioning process consists of a series of polishing steps outlined in Table 1. The resulting images were mosaics made up of 231 (33 \times 7) individually captured tiles at an in-plane resolution of 0.51 μ m/px, and an average spacing of 2.5 μ m/image. The tiles were stitched together using the accompanying software for the Robo-Met machine. In total the process completed after approximately 2 weeks of continuous operation.

2.3. Image analysis

Analysis of the images involved the extraction of fiber positions from each cross-section, then connecting these positions to create fiber paths. Three factors added to the complexity of recognizing fibers in each cross-section. First, the serial sections corresponding to successive layers were imperfectly aligned, which was attributed to inaccuracies in the motion of the kinematic sample holder. Second, as the optical microscope scanned the specimen, uneven lighting created intensity variations within the 64 square-shaped sub-images that formed the total mosaic image. Finally, the optical images were often marred by what appeared to be films of liquid, presumably left over from the cleaning step of the polishing process. The frame misalignments were corrected with the help of ImageJ image stabilization software [39]. The disk and void detection algorithms, described below, were able to handle the local

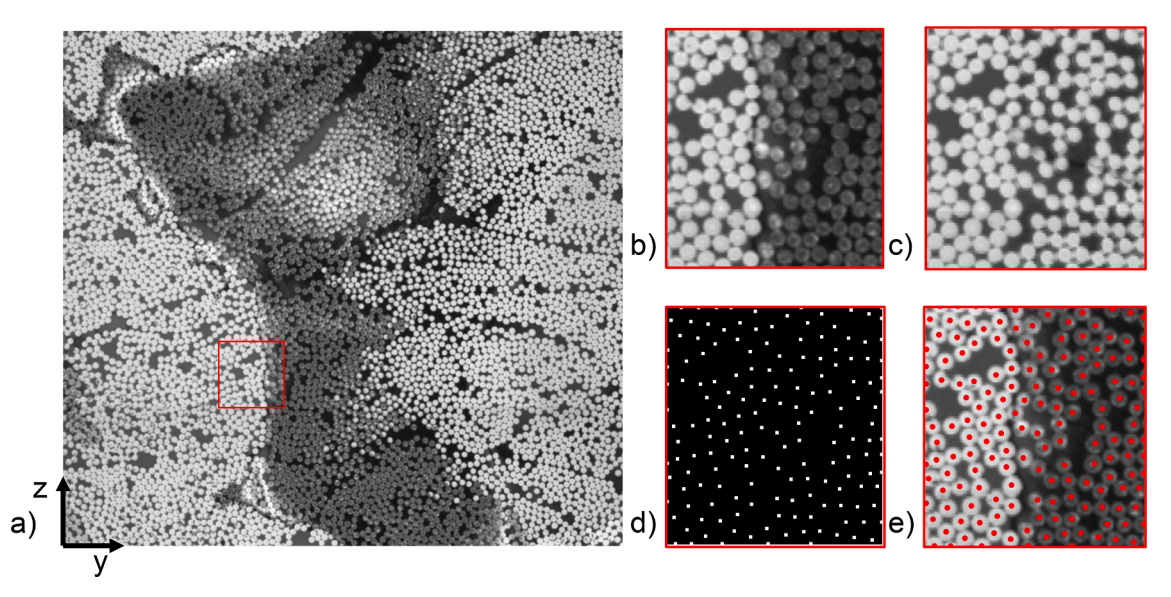


Fig. 2. Image processing method to find fibers despite water droplets on the surface: a) cross section with distortion and sampled region for circle detection, b) eroded greyscale image, c) image with Gaussian filter, d) regional maxima, and e) resulting fibers detected.

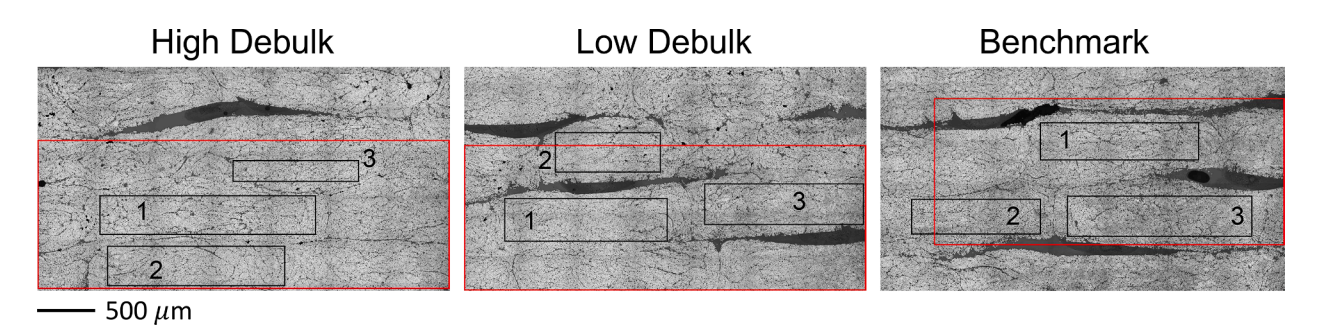


Fig. 3. Cross-sections of the three samples imaged showing the analyzed tows (top) and laminate samples (bottom) used to compare inter-tow to intra-tow fiber behavior. These sections were chosen to avoid the occurrence of blurry regions within the scans.

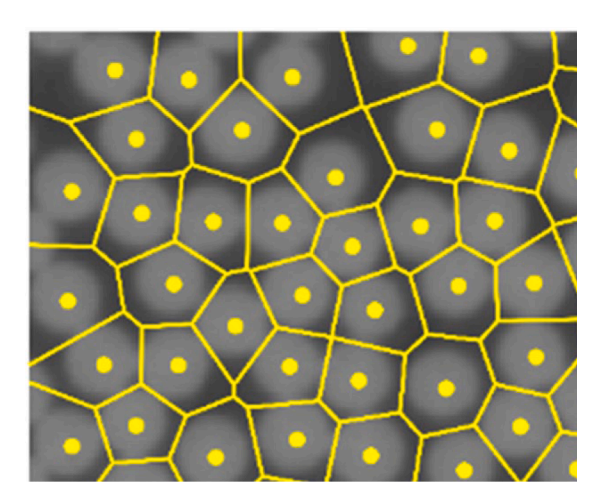


Fig. 4. Cropped section of a micrograph of carbon fibers showing the Voronoi tessellation (yellow lines) of the fiber centers (yellow dots) used to calculate the local volume fraction, v_j^i , of each fiber. (For interpretation of the references to colour in this figure legend, the reader is referred to the web version of this article.)

intensity changes due to uneven lighting.

The correction of irregular hue variations due to liquid spills is illustrated in Fig. 2. The fiber cross-sections in the image foreground

consist of disks with soft, often partially overlapping boundaries. Grayscale images underwent a morphological erosion operation in MATLAB, with a disk structuring element of radius one half of the average fiber radius (3 pixels or 1.51μ m). The images were then binarized, and Gaussian smoothing was applied, with a Gaussian kernel of radius equal to the average fiber radius. This replaces each convex disk by a locally convex function with a unique maximum. To detect the fiber centers, the MATLAB image processing functions "imregionalmax" and "regionprops" were used to locate the centers of each fiber cross-section.

Due to the stiffness of the fibers and the relatively short spacing between images (compared with the fiber diameter), the fiber positions did not vary significantly between sequential cross-sections. This permitted the use of a nearest-neighbor search algorithm from one cross-section to the next to link fibers. The process for detecting and filtering fibers is documented in full within [40].

For each laminate, two types of samples were cropped: regions within a tow and global laminate samples, cropped to exclude regions where fiber locations could not be resolved. In each sample, fiber paths were extracted from both individual tows and macro-scale regions large enough to capture multiple tow parts, referred to here as "laminate" samples (Fig. 3). The purpose of this distinction was to compare metrics of fibers within tows to sample fibers representative of the laminate as a whole.

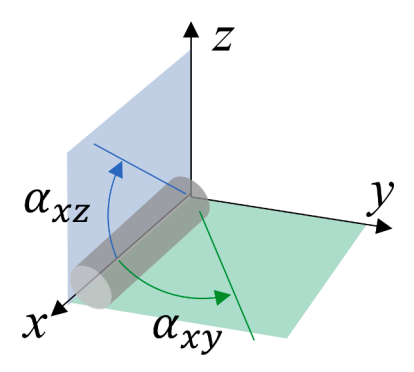


Fig. 5. Diagram of a fiber showing the xz and xy planes in which the off-axiality is measured on, as well as the compaction direction in the z-direction.

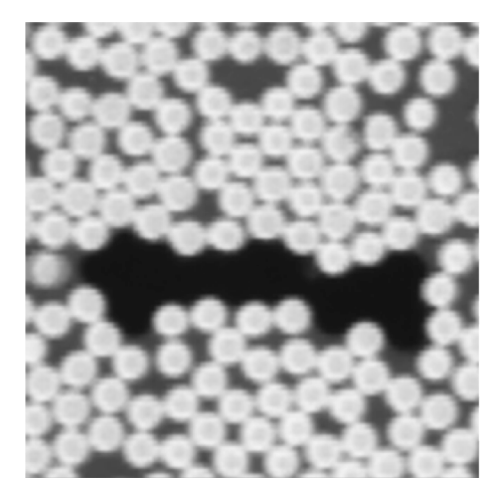


Fig. 6. Picture of a typical void showing sharp contrast between the whitish/gray fibers, gray resin, and black void.

2.4. Metrics

Spatial fiber metrics were measured from the extracted fiber paths in order to observe the effects of debulking on each sample. Additionally,

fiber clusters were detected from the extracted fibers and metrics on the shape and size of the clusters were calculated.

2.4.1. Local fiber volume fraction

The local volume fraction, v_f^i , is the ratio of a fiber's cross-sectional area to the area of that fiber's Voronoi cell in a cross-section (Fig. 4). Unlike the global volume fraction, the local metric provides information on localized regions of high fiber density or sparsity within the sample. The local volume fraction (Equation (1)) can be calculated as

$$v_f^i(x_n) = \frac{\pi r^2}{A_v^i(x_n)} \tag{1}$$

where r is the average fiber radius of all fibers and $A^i_{\nu}(x_n)$ is the area of the Voronoi cell of fiber i at the cross-section x_n .

2.4.2. Fiber unique neighbor change rate

The neighbor change rate $(\dot{\xi}_i)$ is a measure of how often the nearest neighbors of fiber i change along the fiber direction [29]. The neighbor change rate was calculated using the Delaunay triangulation to get each fiber's nearest neighbor in each cross-section. From there, the changes in connectivity from section to section were counted for each fiber.

The pixel error in the fiber detection software employed in this study led to oscillations in the nearest neighbor connectivity from cross-section to cross-section. As a result, certain fibers contain erroneously high total neighbor change counts. To curb this issue, the unique neighbor change rate (UNCR, $\dot{X_i}$) metric was defined. The UNCR is the neighbor change rate where every unique change in nearest neighbor connectivity is only counted once. That is, once a fiber leaves the connectivity array it cannot return.

2.4.3. Fiber Off-Angle

The off-angle, α_{xl} , of a fiber is a measure of the fiber's angular deviation from its intended manufactured direction (x-direction), measured in both the xy and the xz plane (Fig. 5). Measurements taken in the yz plane are omitted from this metric. The process of calculating α_{xl} starts with first linearizing each fiber path by its best linear approximation in 3D. Once linearized, α_{xy} is the angle of the linearized fiber from the x-axis in the xy plane, while α_{xz} is the angle of the linearized fiber from the x-axis in the xz plane.

When a sample is potted in resin for serial sectioning, the orientation

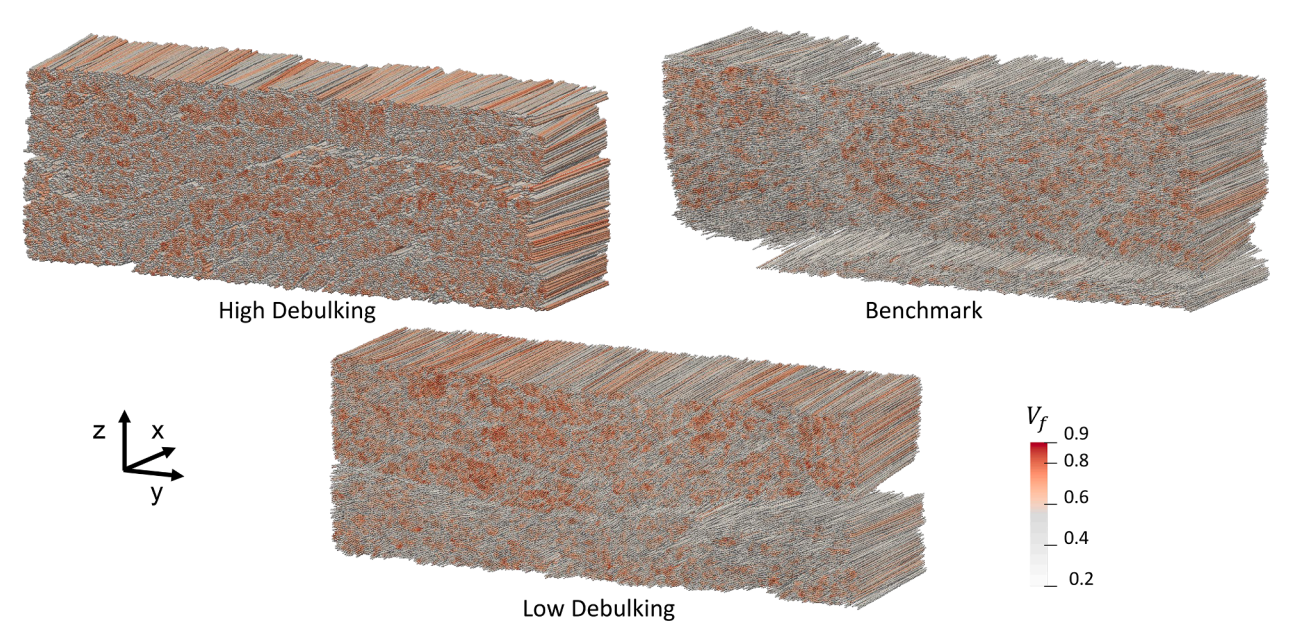


Fig. 7. Select quadrants of the High, Low, and Benchmark debulking laminate samples showing the fibers colored by local fiber volume fraction.

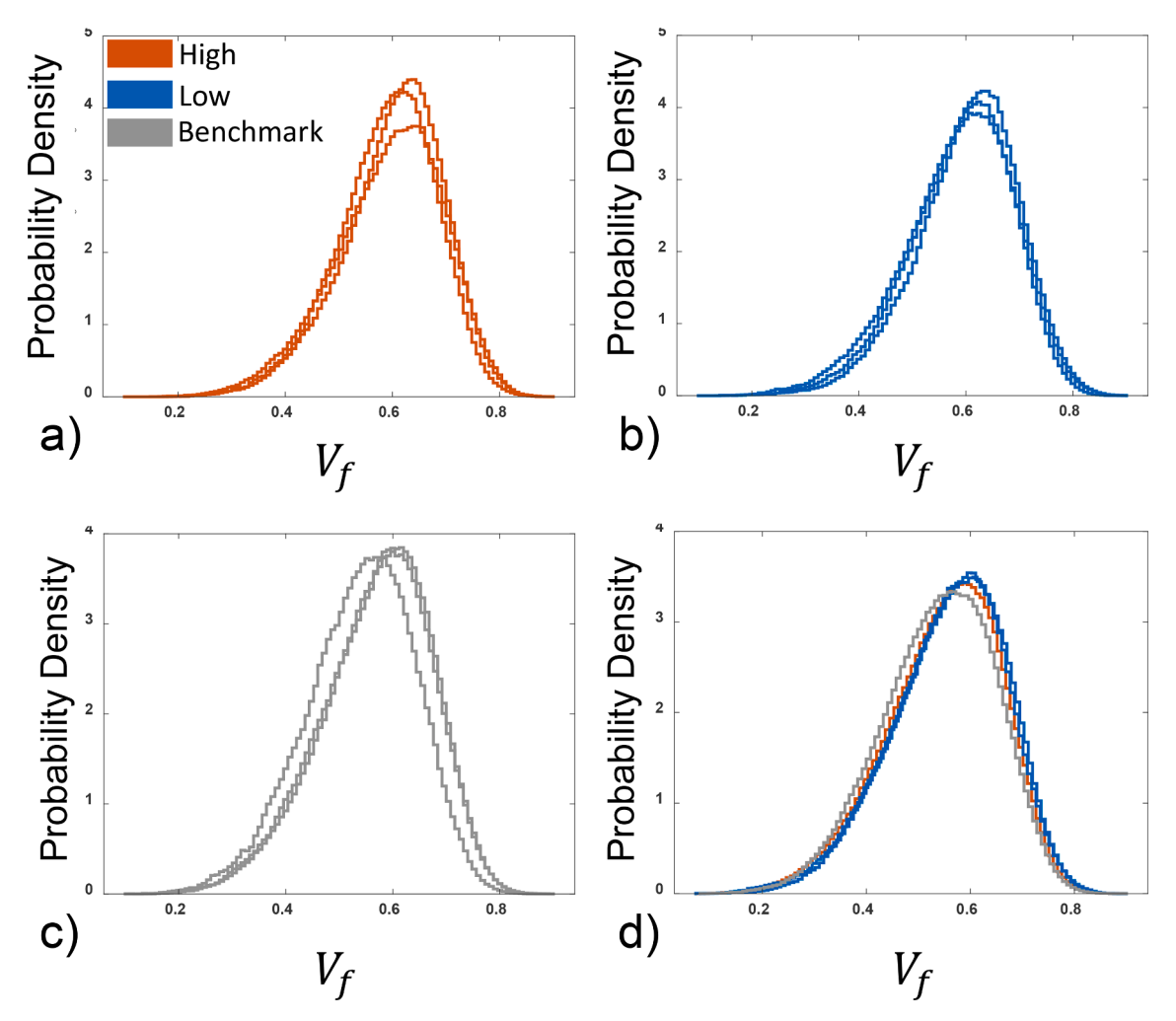


Fig. 8. Local volume fraction, v^i_f , probability density functions of a) high debulk tows, b) low debulk tows, c) benchmark tows, and d) laminate samples from each laminate.

of the sample is often not exactly normal to the viewing plane. This means that the angles of the fibers have an inherent bias in them towards some direction. To remove this bias, the average values for α_{XY} and α_{XZ} were measured and the rotation matrix was used to remove the bias from each sample. This effectively centers the distributions of both α_{XY} and α_{XZ} about the x-axis.

2.5. Fiber clusters

The cluster analysis is a method of describing the tendency for groups of fibers to remain together throughout the volume of fiber reinforced composites. In this study, fiber triads were found using the triangulation of all fiber centers in the first cross-section of an image stack [40]. The cluster metric was defined in terms of the total variation of certain geometric measurements of fiber triads. The total variation of the area, V_A^I , is used here to measure the 3D variation of triad areas within the sample and can be calculated as

$$V_A^l = \sum_{n=2}^N \left| A^l(x_n) - A^l(x_{n-1}) \right| \tag{2}$$

where N is the total number of cross-sections and A^l is the area of triad l at a particular cross-section. It was discovered, however, that it was possible for three fibers to bound a relatively small area but still be spread out. To handle such cases, the total variation of the perimeter, V_p^l , was added as a second criterion and can be calculated as

$$V_P^l = \sum_{n=2}^N \left| P^l(x_n) - P^l(x_{n-1}) \right| \tag{3}$$

where V_P^l is the total variation of the perimeter, and P^l is the perimeter of triad l at a particular cross-section. The final cluster determination is made using the histogram distributions of both criteria. Otsu's method with three bins was then used to threshold V_A^l and V_P^l independently. In this method bin boundaries are set such that the variance within each bin is minimized. In the end, the determination of whether a triad is clustered or not depends solely on the triad's relative location in the distribution of all triads rather than its specific value. The threshold is also invariant of a length scale. The lower thresholds for the area and perimeter variance are then combined in a Boolean operation. For each triad, the values of V_A^l and V_P^l must be below their respective thresholds to be deemed clusters.

Thresholding typically results in a noisy mix of threshold-passing triads, but clusters should be a unique subset of these triads which are aggregated together. To isolate the fiber clusters, a filtering algorithm was created. The intent of filtering is to remove passed triads which were not part of a larger cluster, and include fiber triads which are surrounded by a cluster but did not pass the thresholding. This results in a convergence of fiber clusters, where feature size can be controlled with the filtering method. The basic filtering operation checks whether the neighbors of each triad also passed the thresholds. The algorithm then changes the designation of each triad according to the designation of its

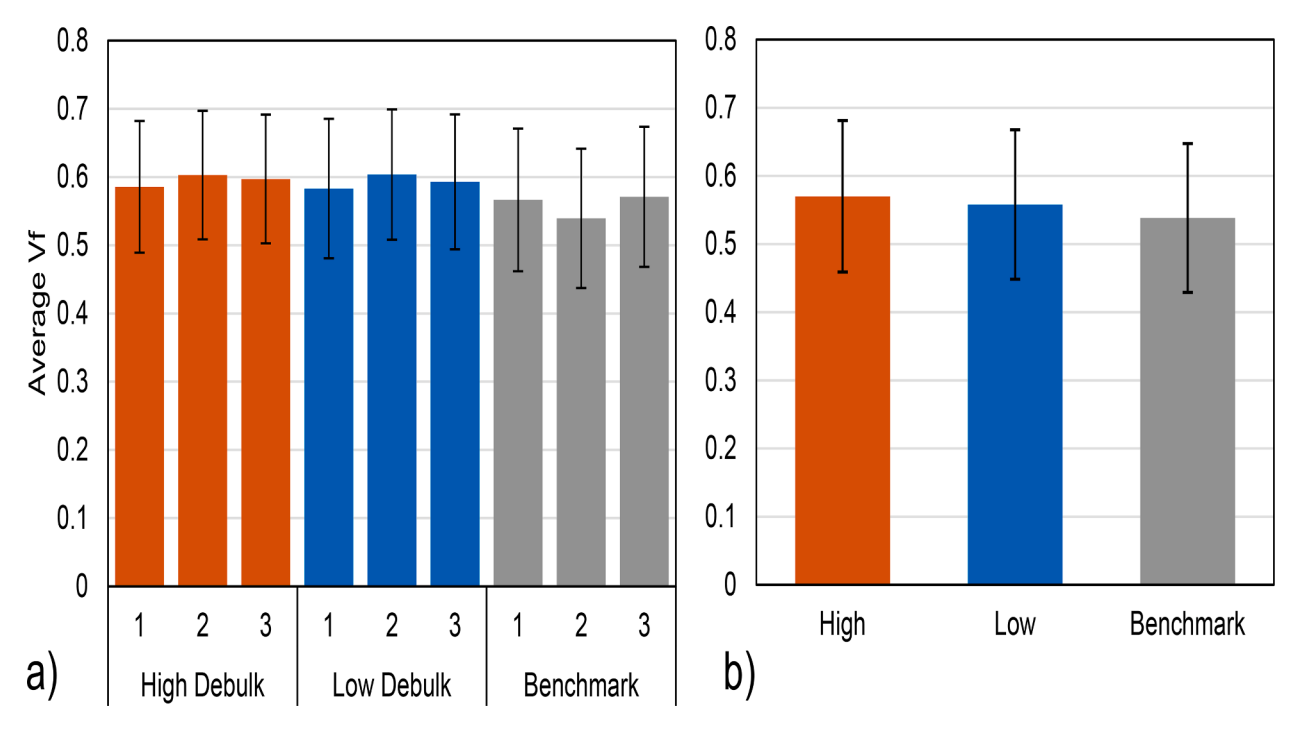


Fig. 9. Average local fiber volume fraction, v_i^i , values for a) tows and b) laminate samples, from each laminate showing standard deviation bars for each.

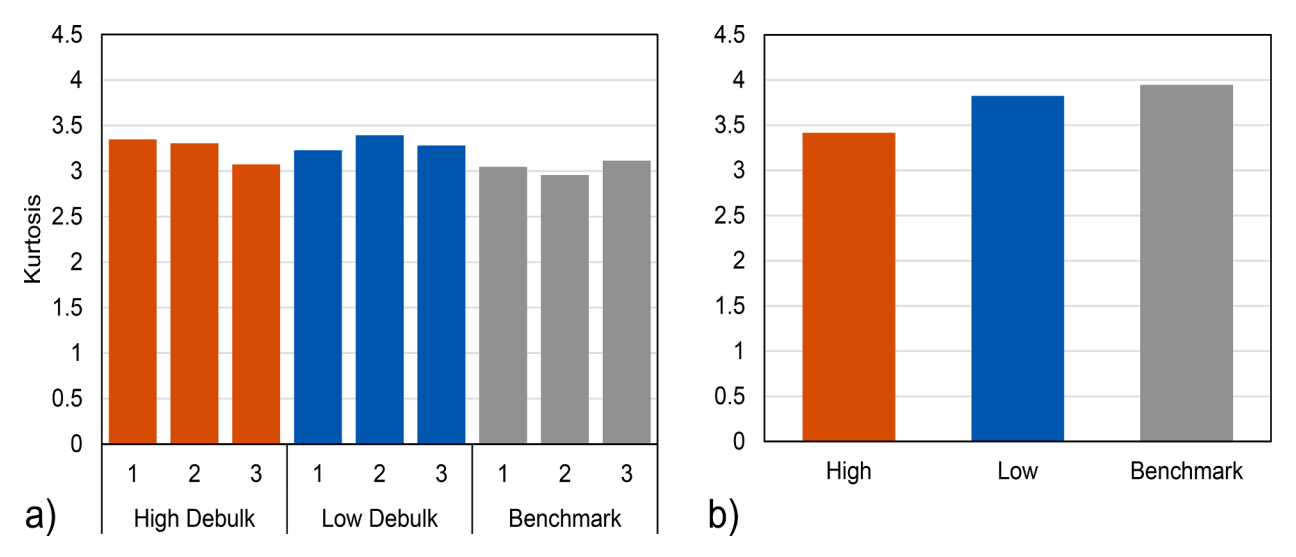


Fig. 10. Average kurtosis of v_f^i for the a) tow and b) laminate samples for each laminate.

neighbors.

Several cluster metrics have been developed to characterize the shape and size of each cluster, as well as the behavior of the fibers within each cluster. For this study, two metrics have been chosen which describe the shape and size of the clusters in the debulk samples. The first of these metrics is the cluster area, which provides info on the size of each cluster in each cross-section.

The second of these metrics is the cluster anisotropy, K, which is calculated from the second moments of area of each cluster. The second moments of area, I_{yy} and I_{zz} , can be calculated for each cross-section (x_n) of a cluster using

$$I_{ii}(x_n) = \sum_{l=1}^{N_i^m} A^l(x_n) d^l_{ii}$$
where $i = y, z$ (4)

where N_t^m is the number of triads in cluster m, $A^l(x_n)$ is the area of triad l

at section x_n , and d_{ii}^l is the distance of the cluster centroid to the center of the triads within the cluster in either the y or z directions. Like the radius of gyration, the moments of inertia are used to understand the geometry of clusters.

The value $K(x_n)$ is used to determine how symmetric the clusters are about both axes, defined as

$$K(x_n) = \sqrt{\frac{I_{yy}(x_n)}{I_{zz}(x_n)}}$$
 (5)

When the values for the moments of inertia are very similar, the value of K is close to one, indicating the clusters are near symmetric about the y and z axes. When I_{yy} is larger than I_{zz} , it means that the cluster is longer in the z direction than in the y direction, and vice versa. The values for K, therefore, give a sense of how symmetric the clusters are about both axes.

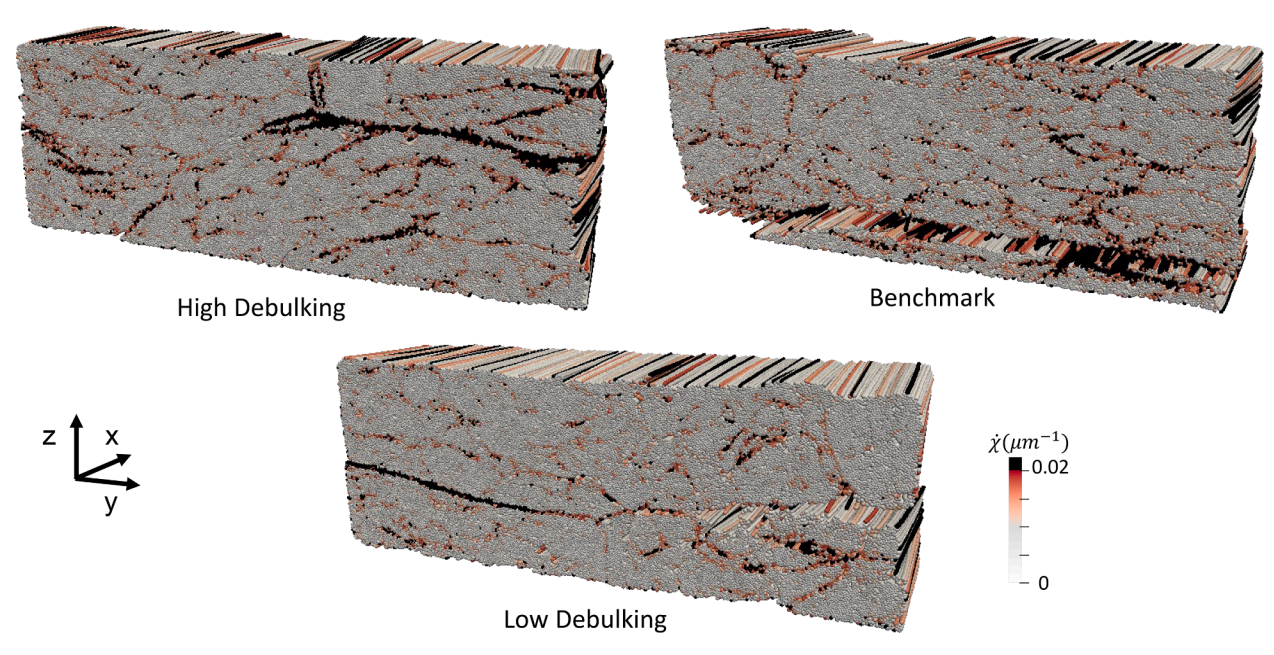


Fig. 11. Select quadrants of the laminate samples showing the fibers colored by unique neighbor change rate, \dot{X}

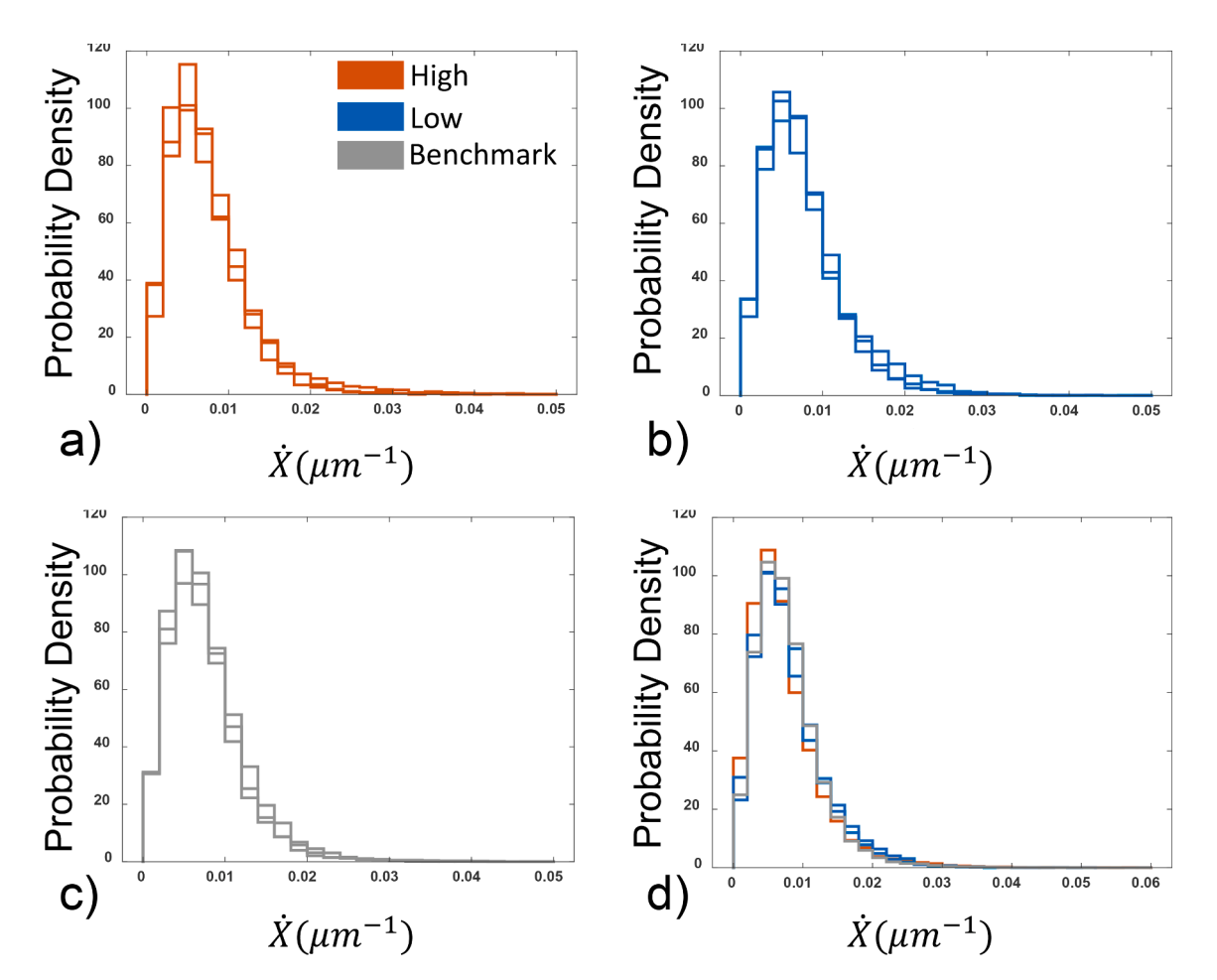


Fig. 12. Unique neighbor change rate, \dot{X} , distributions of a) high debulk tows, b) low debulk tows, c) benchmark tows, and d) laminate samples from each laminate.

2.6. Voids

The void content and distribution of the three samples were computed and contrasted. Voids appear on the grayscale image as

regions of low pixel intensity (lower than either the matrix or the fibers) with sharp boundaries (Fig. 6). They were identified by thresholding the grayscale image and isolating the connected components of regions formed by pixels of low intensity. The center of mass of each void cross-

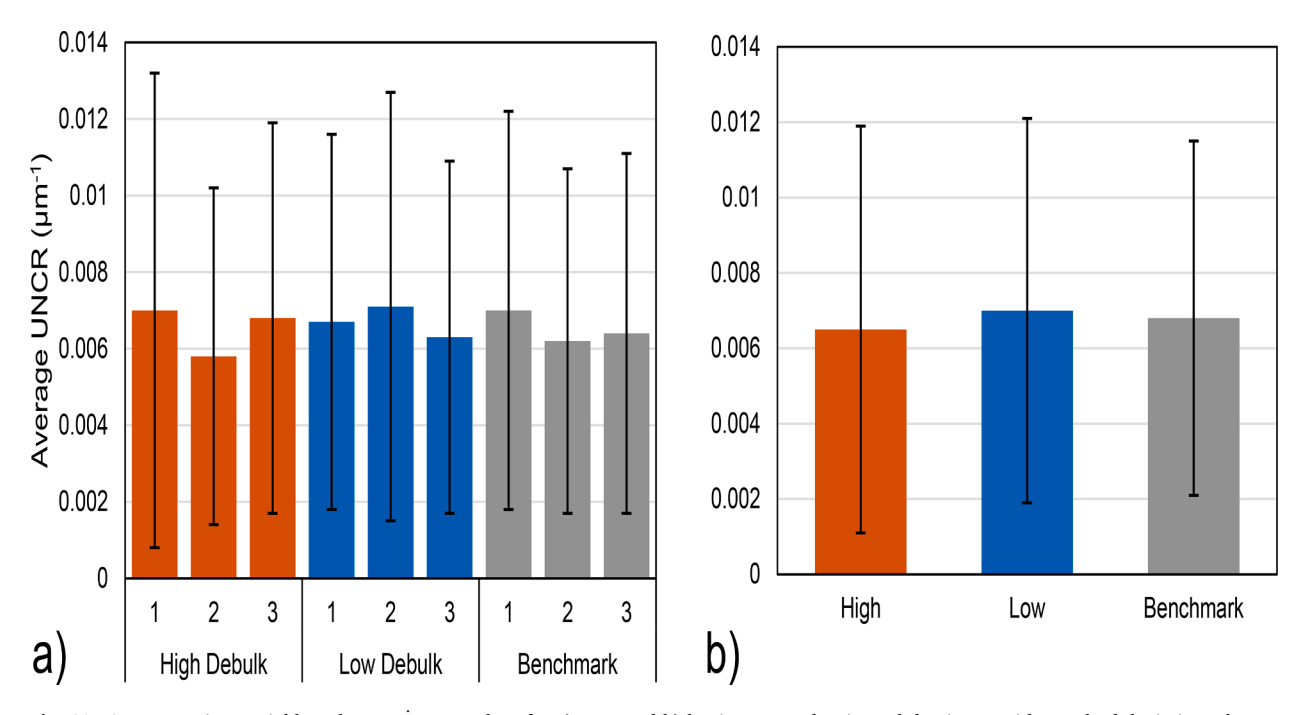


Fig. 13. Average unique neighbor change, \dot{X} , rate values for a) tows and b) laminate samples, in each laminate, with standard deviations shown.

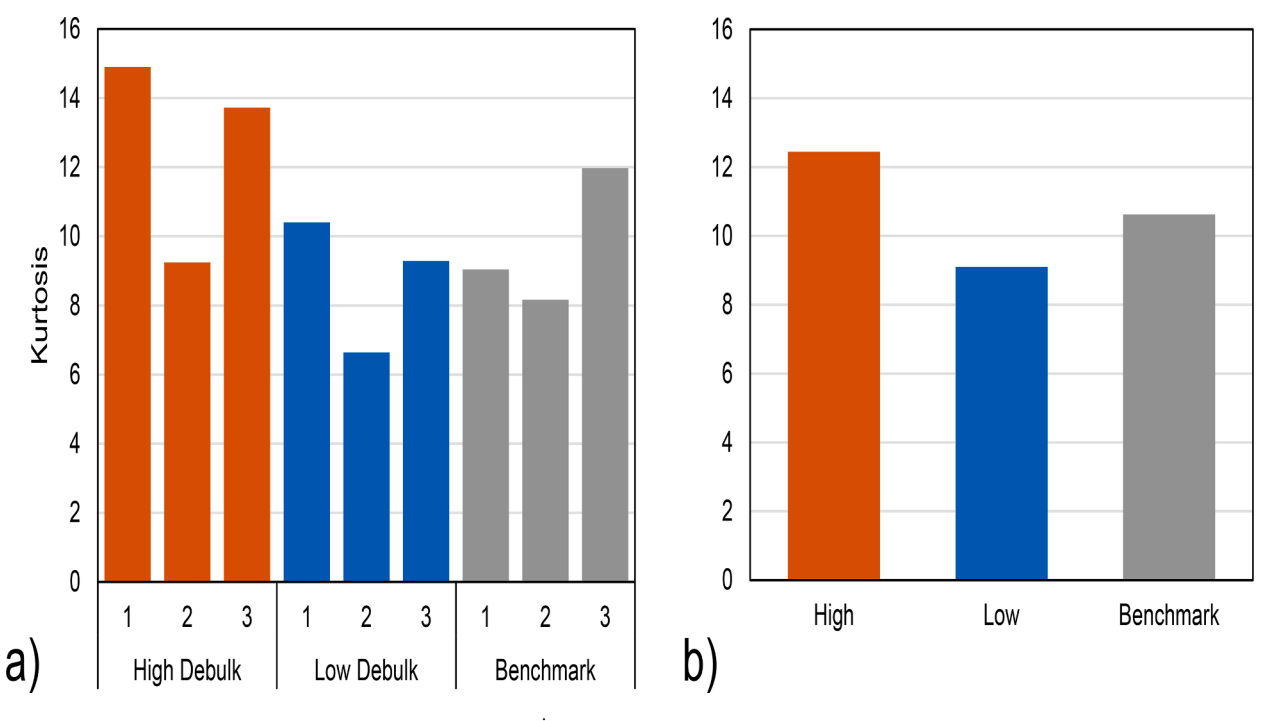


Fig. 14. Kurtosis and average kurtosis of unique neighbor change rate, \dot{X} , for a) tow and b) laminate scale samples showing no clear trend between the entanglement of the fibers and the level of debulking.

section was computed, and centers on successive layers were joined. These computations, as well as voxel-based 3D reconstructions of selected voids, were performed through [27].

Micro-abrasions and voids whose major axes are shorter than five microns are not included in the volumetric and morphological data. As regards structural morphology, the CFRP specimens contain three distinct regimes: intra-tow; inter-tow; and regions surrounding stitches. For the purposes of this investigation, attention was focused on voids within the same tow (intra-tow). The results collected correspond to $2,000 \times 5,000$ pixels, that is, $1.02 \text{ mm} \times 2.55 \text{ mm}$ image segments from

each of the high debulk, low debulk, and benchmark samples, comprising intra-tow regions with no inter-tow interfaces or stitches. The depth of each sample was 199 cross-sections or 500μ m. The void content was found by adding up the total volume of all detected voids and dividing it by the volume of the sample.

3. Results and discussion

Results of each metric were compared across the three levels of debulking to understand the effect of debulking on the resulting

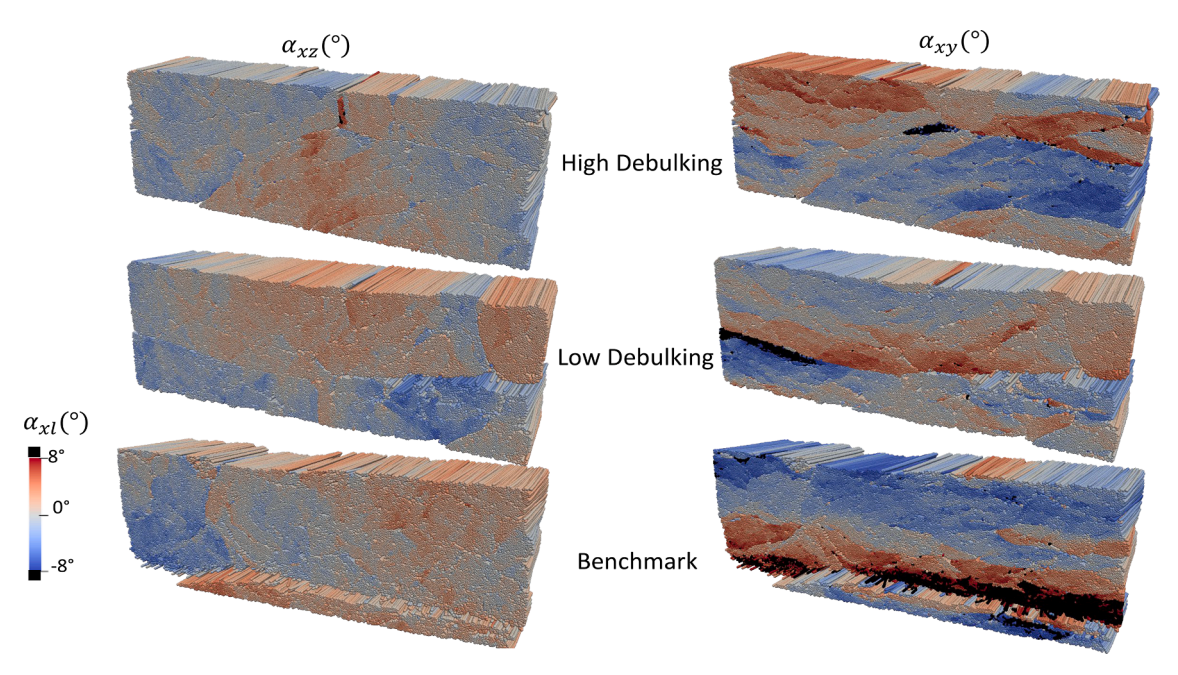


Fig. 15. Select quadrants of the laminate samples showing the fibers colored by off-axiality in both the xz and xy plane, with unusually high values (outliers) colored in black. Tow boundaries can be spotted by looking at the sharp gradients in off- axiality values.

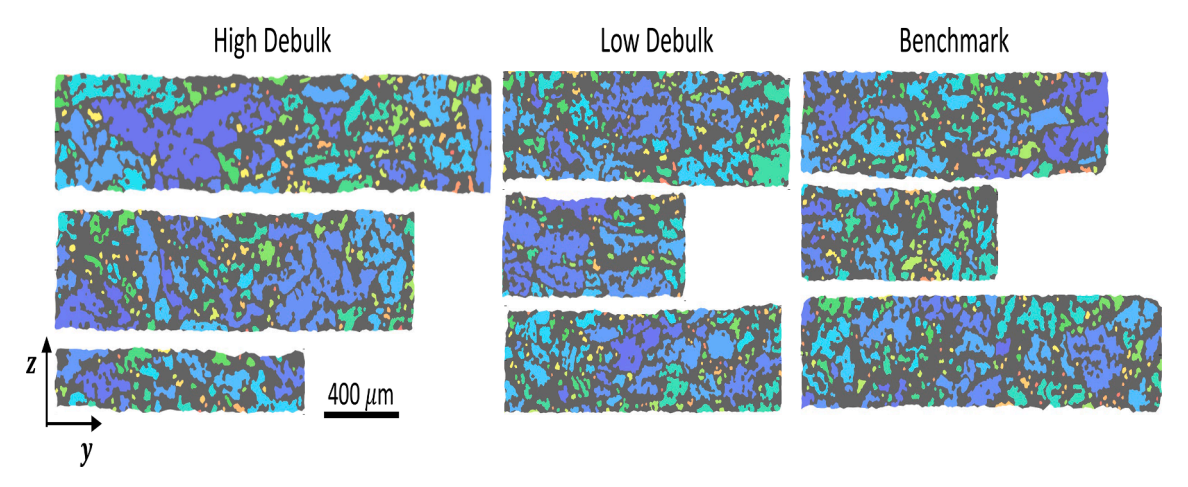


Fig. 16. Results of the of the fiber cluster analysis within three tows each in the three different composite samples. Clusters have been colored based on the order they were detected in while non-clustered triangles remain grey.

microstructure and void content. Visualizations of these metrics were also created by coloring each fiber in the samples by the results of each metric. A cluster analysis of each sample was also performed.

3.1. Fiber metrics

3.1.1. Local fiber volume fraction

The local fiber volume fraction, v_f^i , is a measure of the area of a fiber to the area of its Voronoi cell. This formulation of volume fraction can be used to obtain local data for each fiber in every cross-section, and gain insight into the spatial density of the fibers. Reconstructions of the laminate samples, colored by local volume fraction, can be seen in Fig. 7. These reconstructions show visually how the fibers manifest themselves into tight islands (red regions) surrounded by more matrix rich regions (gray fibers) in all three samples. It can also be seen that the number of more matrix rich regions is clearly higher in the benchmark sample than the other two.

The histograms for the local volume fraction in each analyzed tow and the laminate samples are shown in Fig. 8. The shapes of the high

debulk and low debulk tow histograms are similar in terms of magnitude at the mode and distribution. The benchmark tows, however, have a slightly lower probability density than any of the tows in the other laminates. The location of the modes for the benchmark tows all occurred below 0.6, while the modes of the other laminates occurred above 0.6 fiber volume fraction. The histograms of the laminate samples show a similar trend, with the high and low debulk distributions being similar and the benchmark sample being lower at the mode.

The average local fiber volume fractions of the three tows and laminate samples analyzed in each laminate are shown in Fig. 9, with standard deviations. Results suggest that the debulking procedure was most noticeable between the benchmark sample to the low debulking steps in terms of increasing compaction. The overlap of the standard deviations is large, however, which suggests that the differences in the mean local volume fraction are minimal. One of the areas where a difference might occur is at the tails of the distributions, specifically the lower end, where fibers have more resin surrounding them and thus more space to meander prior to infusion. The fibers at the tails of the distributions are referred to here as outliers.

M. Schey et al. Composites Part A 165 (2023) 107364

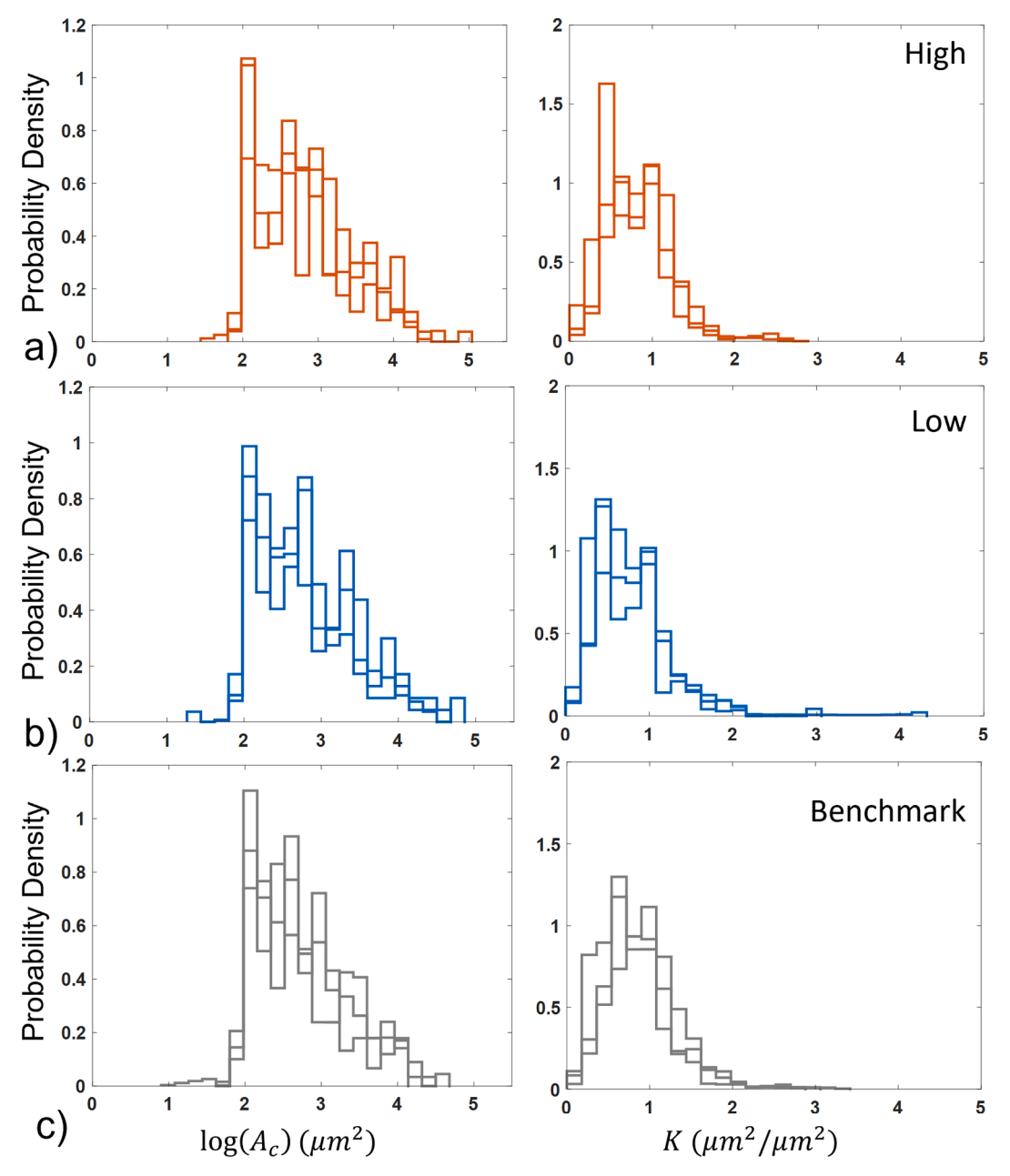


Fig. 17. Log of cluster area, A_c , and ratio K representing the symmetry of each cluster for a) high debulk, b) low debulk, and c) benchmark tows.

Looking at the colored reconstructions of the fibers shows that the volume fraction appears to decrease around the tow boundaries, which is not captured in the cropped tow sample images (Fig. 7). This could partially account for the slightly higher fiber contents in the tow data compared to the laminate samples. Similarly, looking at the kurtosis of the tows does not provide much insight into the actual effects of debulking on the samples (Fig. 10a). Fibers inside each tow were clumped together prior to debulking or infusion, which could have lessened the amount of outliers that exist within the sample. The laminate scale, however, shows a clear trend of increasing kurtosis with decreasing amounts of debulking (Fig. 10b). In the laminate sample pictures, many areas of lower volume fraction can be seen around the boundaries of tows. This result suggests that, while debulking influences the average local volume fraction for the three samples, it also has noticeable effect on the outlier fibers in each sample.

3.1.2. Unique neighbor change rate

The unique neighbor change rate, \dot{X} , is a measure of the number of

unique changes in a fiber's nearest neighbors along the fiber's length. Unique changes refer to the fact that each neighbor change is only counted once. Straight fibers surrounded by misaligned fibers may have just as many neighbor changes as misaligned fibers surrounded by straight fibers. Reconstructions of the laminate samples, colored by unique neighbor change rate, are shown in Fig. 11. These figures show that the unique neighbor change rates are highest at the boundaries between tows. Within the tows, the uniformity of the unique neighbor change rate for the fibers is much higher. The main reason for this is that the orientation of the tows themselves are not uniform, but the orientation of the fibers within each tow is consistent as illustrated by the off axiality metric later on (Fig. 15).

The probability density function for the unique neighbor change rate was consistent across all tows and laminate samples, and across the levels of debulking (Fig. 12). The similarities seen across tows and laminate samples for each level of debulking suggest that the level of entanglement is a constant throughout the sample if the population size is at least as large as the smallest tow used in this analysis. It is unknown

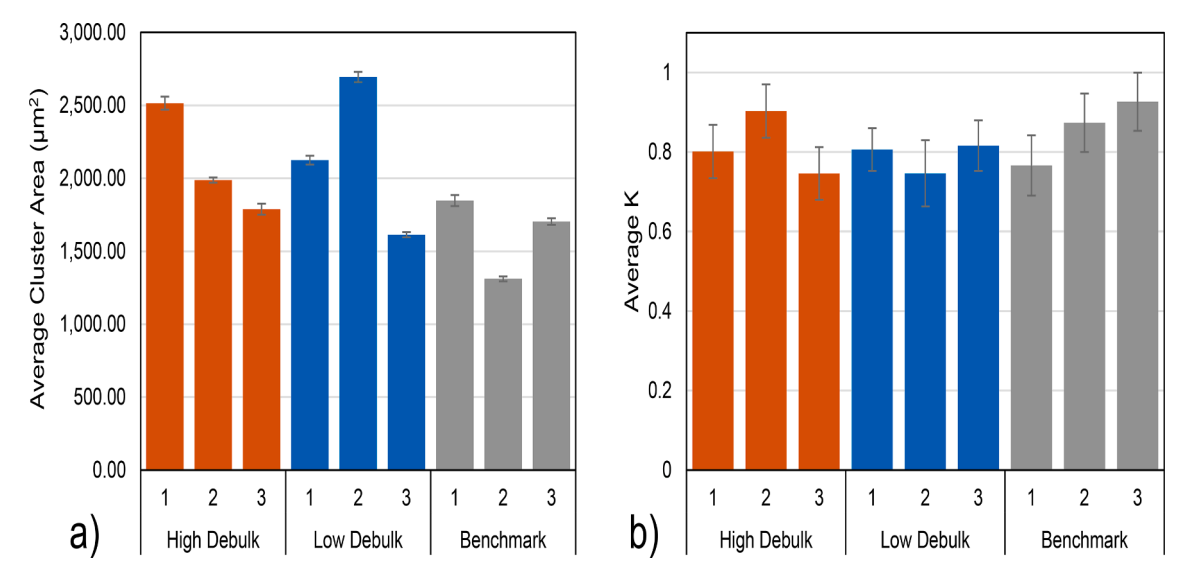


Fig. 18. Bar plots of a) average cluster size and b) average K value representing the symmetry of each cluster for each tow in each laminate, showing standard deviations.

Table 2
Results of void analysis.

Laminate	# Voids	Max Volume (μ m³) x10 ⁴	Min Volume (μ m ³)	Average Volume $(\mu \text{ m}^3) \text{ x} 10^4$	Median Volume (μ m ³)	Volume STD (μ m³) x10 ⁴	LongestVoid (μm)	Void Content $\left(\frac{\mu m^3}{\mu m^3 x 10^6}\right)$
High	496	86.9	9.10	1.51	95.6	6.25	442.5	5831.36
Low	301	13.5	7.80	0.521	48.8	1.73	232.5	1236.70
Bench	347	8.93	7.80	0.00541	27.3	0.0087	12.5	14.58

whether the unique neighbor change rate distribution would change significantly at smaller scales, or what this minimum size would be.

Regarding the level of debulking, the similarity of the unique neighbor change rate across all levels of debulking suggests that the entanglement (as measured by the unique neighbor change rate) is unaffected by the level of debulking applied to the fibers. Given this finding and the finding that local volume fraction is affected by the level of debulking suggests that relative fiber positions, i.e. a fiber's location relative to it's neighbors, remains unaffected while the spatial distance between neighbors decreases as a function of debulking.

The average values of the unique neighbor change rate are shown in Fig. 13, with standard deviations. Across each layer the tows seem to show no clear trend in terms of the debulking level versus the number of neighbor changes. The standard deviations for each sample are very large when compared to the averages, and overlap greatly from tow to tow

The kurtosis for the UNCR was much higher than for the fiber content (Fig. 14). Unlike the local volume fraction, which is bounded by the maximum and minimum fiber density of the sample, the UNCR is controlled by the relative orientation of each fiber to its nearest neighbors. This means that the upper bound of the UNCR metric is not as physically restricted as the local volume fraction (which is restricted to ~ 0.9 , in the tightest fiber packing possible). It is feasible that a fiber's path could cut across many different fibers from the beginning to the end of the scanned section. This permits outlier fibers to be more numerous, which could explain the increased number of outliers. The absence of any relationship between debulking magnitude and UNCR suggests that debulking does not change the entanglement of the fibers, but instead increases the density while holding the entanglement the same.

3.1.3. Off axiality

The off-axiality of a fiber in a laminate is a measure of that fiber's deviation from the intended (0° for the debulk samples) direction for the

layer it belongs to. Coloring the fibers in 3D using the values for off-axiality shows that the laminate samples in all three plates are not uniform in their orientation (Fig. 15).

In many cases, clear boundaries between tows and even plies can be seen due to the sharp gradients seen in the sample. This shows that the tows in each sample are not necessarily oriented the same way in a given plane. Individual plies also appear to orient themselves differently from other plies. It is possible that, with the results from the kurtosis of the local volume fraction distribution in mind, the rise in volume fraction outliers is in part due to the misorientation of the tows to one another. Tows being oriented at differing angles likely prevents the fibers from neighboring tows to nest within each other, creating regions of low density between them.

Comparing the two planes, it can be seen that the fibers are oriented more homogeneously in the xz plane than in the xy plane. In other words, the xz plane has a narrower distribution of angles (i.e. the extremes are closer together) and contains fewer outlier fibers, or fibers outside the plotted bounds. This result suggests that fiber meandering is most typically restricted to the xy plane, meaning that large fiber misorientation occurs in the direction normal to the direction of compaction. There does not appear to be, however, any indication that the level of off-axiality is affected by the level of debulking applied.

3.2. Cluster metrics

The cluster analysis is used to identify bundles of fibers that are oriented together within a given sample. The results of the cluster analysis for all three tows in the high debulk, low debulk, and benchmark laminates are shown in Fig. 16. In these plots, each cluster is colored differently depending on the order in which the cluster was detected. Looking at the plots of the clusters it can be seen that, in general, the clusters are longer in the direction normal to compaction (y direction).

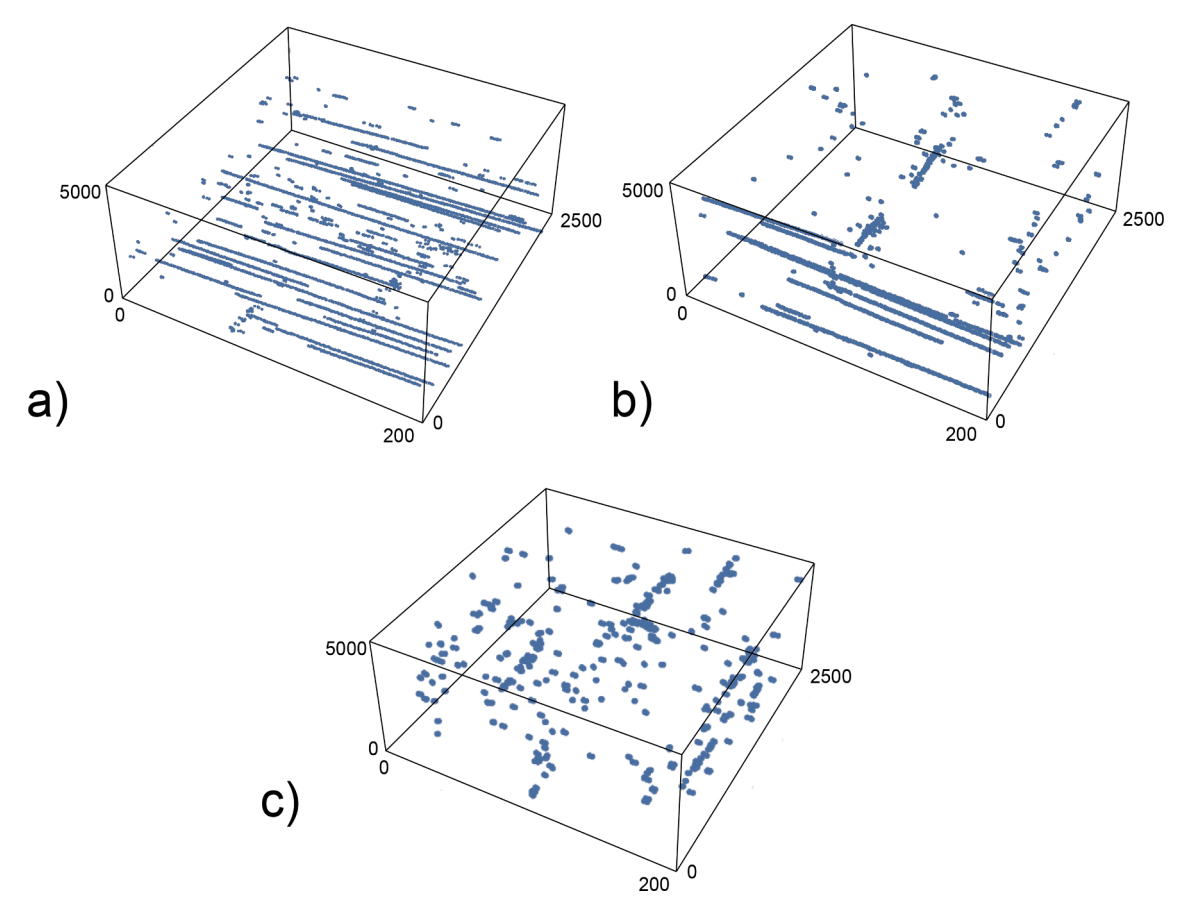


Fig. 19. 3D scatter plots of voids in a) high debulk, b) low debulk, and c) benchmark laminates.

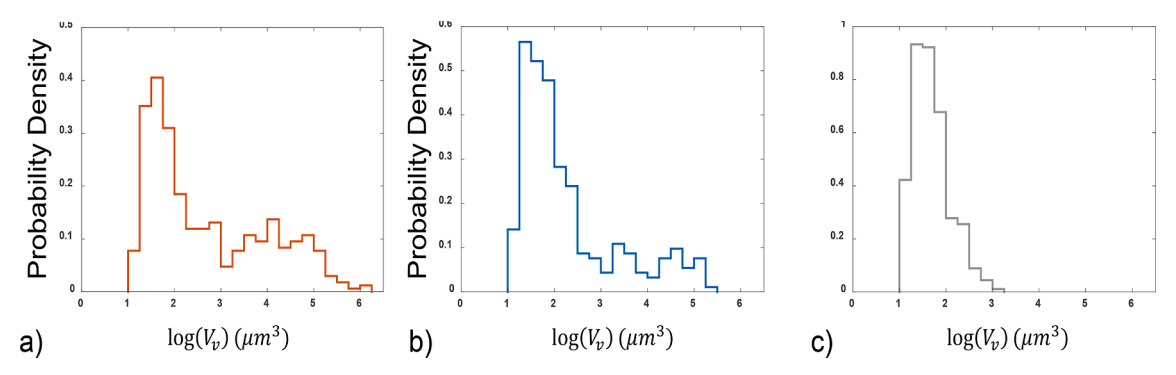


Fig. 20. Histogram of the Log of void volumes for a) high debulk, b) low debulk, and c) benchmark samples.

The histograms for the log of the cluster area and the K ratio are shown in Fig. 17. The cluster areas most often occur on the order of 10^2 to $10^3~\mu$ m 2 for all tows in all samples. One observation about the area of the clusters is that the larger samples tended to have larger clusters. This makes sense because larger samples have more fibers and thus more potential to be part of a cluster. Despite this, the mode of the cluster areas seems to not depend on the size of the sample at all. That is, the most common cluster size range appears constant across both large and small tows.

The K ratio is a measure of the symmetry of a cluster about both the y and z axes. When K is below 1 the cluster is longer in the y direction, and when K is above 1 the cluster is longer in the z direction. The histograms for the K ratio show that the majority of clusters in each tow have a K value lower than 1, further confirming that the clusters tend to be longer in the y direction, i.e. normal to the compaction direction.

The average values for cluster area are shown in Fig. 18a. The

clusters in the high and low debulk tows tended to be larger than the clusters in the benchmark sample. The standard deviations were also extremely low for each measurement when compared to the average value. This result suggests that the size of the clusters in each tow could be related to the level of debulking applied. It would make sense that the size of fiber clusters would be larger with the more debulking steps. The increased debulking steps, in theory, should decrease the distance between neighboring fibers. This decrease in distance would directly affect the variation in area and perimeter for each cluster, causing more fiber triads to pass as clusters.

The average values for ratio K are shown in Fig. 18b. Again, the vast majority of clusters have a K ratio lower than one. There is no apparent trend with respect to the level of debulking, besides the fact that all debulked samples have an average below 1, even when the standard deviation is considered. This suggests that the shape of the fiber clusters within tows is independent of the level of debulking.

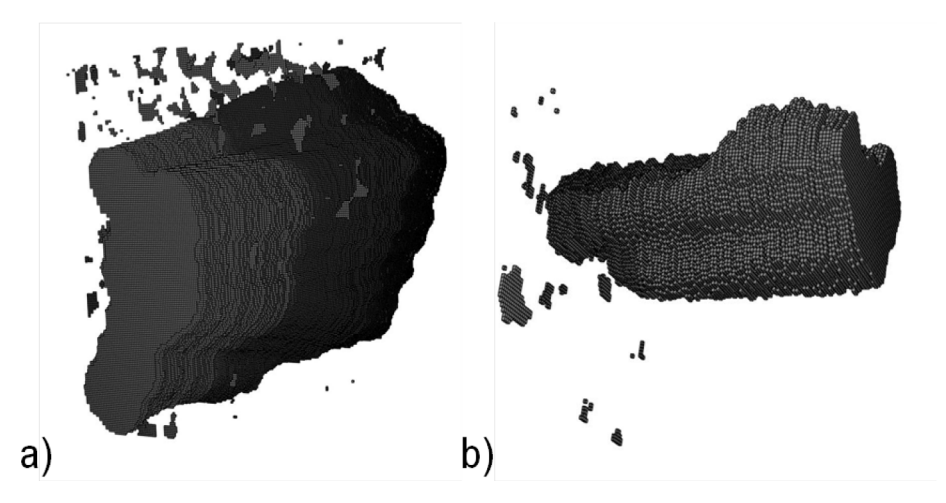


Fig. 21. Voxel reconstruction of the largest voids for the a) high debulk and b) low debulk samples.

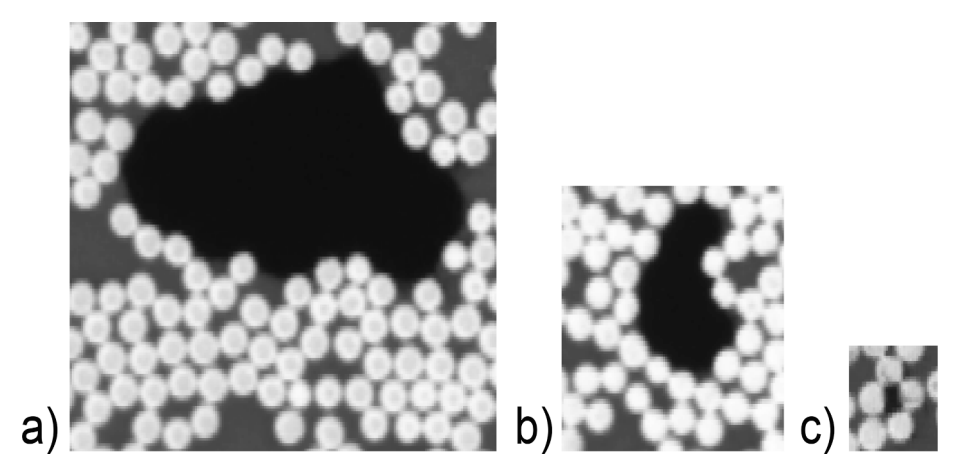


Fig. 22. Portraits of maximal void 2D cross-sections for the a) high debulk, b) low debulk, and c) benchmark samples. Voids are the darker colored regions.

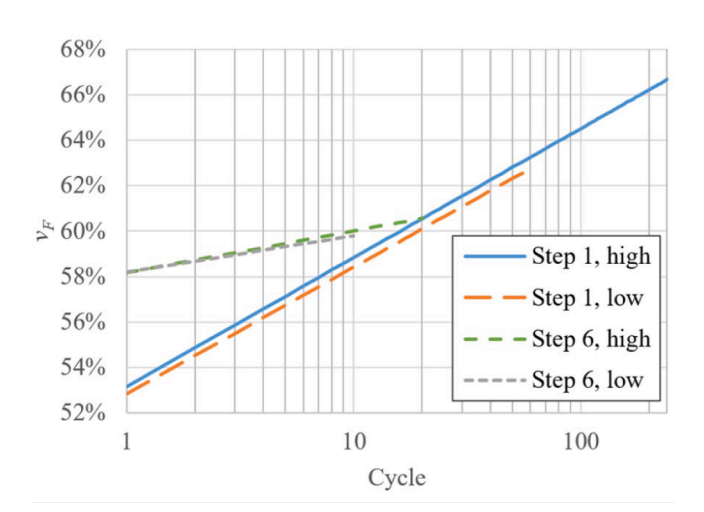


Fig. 23. Maximum recorded fiber content in each compression cycle, during initial (step 1) and later cycle B debulking (step 6), for a sample subjected to a "low" cycle count, and another sample subjected to a "high" cycle count.

3.3. Voids

Voids form within fiber reinforced materials during the resin infusion process. Results of the void analysis are shown in Table 2 including the

quantity of voids in the image, as well as various size metrics.

The data confirms the hypothesis that increased debulking increases both the void content and the average void size of VI-manufactured CFRP. Moreover, with increased debulking, the growth in the number of voids, while noticeable, is dwarfed by the effect of increased void size. The overall increase in void content seems to be entirely due to increases in the mean void volume and the appearance of larger voids. This can also be seen visually by plotting the centerline plots of the voids for each laminate (Fig. 19). High aspect ratio, i.e. long voids begin to appear with a moderate amount of debulking, and are common with the higher degree of debulking.

The histogram of logarithms of void volumes suggests that the distribution of void volumes is approximately lognormal around its mode, but there is insufficient data to ascertain the nature of tail distributions and outliers (Fig. 20). Microvoids, which are defined here as voids smaller than the diameter of a fiber, were not included in the statistics due to the difficulty of reliably separating them from image noise, while voids of exceptional length were cut off by one end or the other of the specimens. The 3D reconstruction of these voids suggests that they are macroscopic, perhaps 1 mm in full length.

Voids are approximately prolate spheroids in shape, with major axes parallel to the fiber direction (Fig. 21). Unlike those of microvoids, however, the cross-sections of macroscopic voids are clearly not convex. The indentations are due to the presence of nearby fibers. Portraits of voids at their widest cross-sections confirm that they are almost entirely surrounded by a tight perimeter of fibers (Fig. 22).

The interface between the voids and nearby matrix-rich areas is

negligible, and the diameter of void cross-sections far exceeds the mean spacing between adjacent fibers. The two phases seem to exist in an equilibrium of forces, with both the fibers constraining the void shape by e.g. filament bending stiffness, and the void pushing the fibers apart by the fluid pressure of the bubble. It is left for further research to understand the fluid mechanics leading to the formation of these macroscopic voids.

4. Summary and conclusions

Debulking is typically done to improve the compaction of carbon fibers prior to infusion, thus improving the performance of cured fiber reinforced composites while avoiding more expensive manufacturing techniques. While limited work has been done in the past to study the effects of debulking on the void formation within manufactured parts, no previous work has studied the effect of debulking on the resulting fiber and void microstructure after the high number of debulking cycles typical to industry.

Metrics were employed which permit the study of the spatial and structural distribution of fibers and voids. Comparison of the fiber local volume fraction distribution showed that the level of debulking seemed to increase the mean local volume fraction of carbon fibers slightly, but the overlap of the standard deviations for both the tow and laminate samples casted doubt on the significance of these differences. A clearer comparison between the different levels of debulking came from the kurtosis of the local fiber volume fraction data for the laminate samples. These results showed that the number of outlier fibers in terms of local fiber volume fraction increased as the level of debulking decreased. This suggests that one of the true effects of debulking is not an increase in the mean density of fibers within the sample but rather an increase in the density of fibers with unusually low local volume fraction values, such as those which occur at more resin rich regions at the boundaries of tows and plies.

The unique neighbor change metric was used to see if the level of debulking influenced the relative position of each fiber to its nearest neighbors. The probability density functions across the tow and laminate samples were extremely similar, suggesting that the level of entanglement is a constant throughout the sample if the population size of fibers is at least as large as the smallest tow sample analyzed. Further work needs to be done to quantify whether the distribution of the unique neighbor change rate observed changes at smaller sample sizes and what this size would be. No clear relationship was observed between the unique neighbor change rate and the level of debulking. This suggests that the relative fiber positions do not change as a function of the level of debulking applied to the dry fibers prior to infusion.

The cluster analysis was performed to see whether the level of debulking had any effect on the fiber clustering present within the sample. The clusters present in all samples were longer in the direction normal to compaction. The cluster size was higher in the debulked samples.

The void content and size of voids significantly increased with the level of debulking, and was the most pronounced difference between the high, low, and benchmark samples. The reconstruction of the voids showed that they are non-convex, and always surrounded by fibers. The surrounding fibers suggest that the presence of the voids is due to the tight packing of the fibers caused by the level of debulking. It is unclear yet whether the voids caused any kind of deviation of the fiber paths. Further analysis needs to be done to see whether the voids present change the orientation of the fibers.

The debulking process is widely used as an alternative to manufacturing methods which compact fibers at a higher cost. Research has shown that the process of debulking can produce favorable volume fractions of fibers, but at the cost of slower infiltration and potentially increasing voids. The analysis of voids and void content as a function of debulking is an important step in the endeavor to understand the structural effects of debulking itself. Additionally, it is important to

understand the resulting microstructure of any manufacturing process so that ties between manufacturing and performance can be made. The results presented here are meant to further understand the effects of debulking on the final microstructure of unidirectional laminates. Identifying the effects of debulking on the resulting microstructure through rigorous analysis and metrics will hopefully bring research a step closer to tailoring manufacturing processes and producing optimal composite parts.

CRediT authorship contribution statement

Mathew Schey: Software, Formal analysis, Investigation, Visualization, Writing – original draft, Writing – review & editing. Tibor Beke: Formal analysis, Investigation, Visualization, Writing – original draft. Kyle Owens: Investigation, Formal analysis. Andy George: Conceptualization, Investigation, Resources, Methodology, Writing – original draft, Writing – review & editing. Evan Pineda: Conceptualization, Resources, Supervision, Funding acquisition. Scott Stapleton: Conceptualization, Methodology, Writing – review & editing, Supervision, Project administration.

Declaration of Competing Interest

The authors declare that they have no known competing financial interests or personal relationships that could have appeared to influence the work reported in this paper.

Data availability

Data will be made available on request.

Acknowledgements

This work is based upon work supported by the National Science Foundation and Air Force Office of Scientific Research under grant number IIP1826232. Any opinions, findings, and conclusions or recommendations expressed in this material are those of the author(s) and do not necessarily reflect the views of the National Science Foundation.

The authors would like to thank Richard Martin at the NASA Glenn Research center for their funding, time, and assistance with the Robo-MET serial sectioning machine. The authors would also like to thank Valentin Boutrouche of the University of Massachusetts for his contributions to the visualizations used in this work.

Notice of Copyright Information

This manuscript is a joint work of employees of the National Aeronautics and Space Administration and employees of University of Massachusetts Lowell and Brigham Young University with the National Aeronautics and Space Administration. The United States Government may prepare derivative works, publish, or reproduce this manuscript and allow others to do so. Any publisher accepting this manuscript for publication acknowledges that the United States Government retains a non-exclusive, irrevocable, worldwide license to prepare derivative works, publish, or reproduce the published form of this manuscript, or allow others to do so, for United States government purposes.

Appendix

Debulking procedure

Fig. 23 shows the maximum v_F (global) recorded (i.e. minimum sample thickness) during each cycle for debulking steps 1 and 6, in which cycle A and cycle B debulking cycles (respectively) were performed on the "low" and "high" debulk ply-stacks, with more cycles

performed on the "high" sample than "low.".

During the very first debulking cycle (step 1), the two samples are initially at a similar, low fiber content of just under 54 %, and this increases by a logarithmic trend with each cycle, i.e. the magnitude of the increase (slope of this graph) decreases with each cycle. Two days later, the first Cycle C test was performed, and then six days after that, another Cycle C test was performed to evaluate the rate of "springback," i.e. how fast does the fiber rearrangement reverse into a less nested state. Then the Cycle B debulking was performed in Step 6. As seen in Fig. 23, in that step, the two samples again show approximately the same fiber content during the first cycle B debulk and increase in fiber content at nearly the same rate with each cycle. The higher initial fiber content (58 %) shows that the earlier debulking did induce fiber nesting. But the lack of difference between the low and high samples suggests that any difference in the quantity of Cycle A debulking (between the low and high samples) was negated by the springback over those 8 days delay and / or more significant nesting occurring during the identical Cycle C testing.

Vacuum infusion process

Three laminates were manufactured by vacuum infusion under a vacuum bag, using a layer of flow media over the top to accelerate the filling time. Two of the laminates were prepared from the "low debulk" and "high debulk" samples from the debulking experiments, which were infused shortly after the last debulking cycle. The third laminate was prepared from a ply-stack straight from the fabric roll, with no debulking, referred to as the "benchmark" sample.

An inlet channel was situated across one of the edges of the sample to create approximately uni-directional flow across the square preform. Flow media covered all the surface of the preform except for an approximately 20 mm wide perimeter along the vent-side of the preform as well as the sides perpendicular to the flow direction. The resin was mixed, then degassed for 15 min before infusion. The applied pressure gradient was 86 kPa.

The resin viscosity was measured just prior to infusion with a Brookfield viscometer, and was approximately 360 mPa·s for all three infusions. Thermocouples verified that the epoxy resin, both in the pot and in the mold, remained at nearly a constant temperature, approximately 21° C.

After filling the preform, the inlet pipe from the resin pot was clamped shut and the sample left under vacuum until the part was cured. Upon demolding, some dry areas were noticed on the rigid mold-side of the high-debulk laminate. This denotes the tortuous path of the resin from the flow media through the thickness of a uni-directional weave, with relatively low permeability compared to other reinforcements, and exacerbated by debulking.

References

- [1] Williams C, Summerscales J, Grove S. Resin Infusion under Flexible Tooling (RIFT): a review. Compos A Appl Sci Manuf Jan. 1996;27(7):517–24. https://doi.org/ 10.1016/1359-835X(96)00008-5.
- [2] S. F. M. de Almeida and Z. dos S. N. Neto, "Effect of void content on the strength of composite laminates," *Composite Structures*, vol. 28, no. 2, pp. 139–148, Jan. 1994, doi: 10.1016/0263-8223(94)90044-2.
- [3] Liu L, Zhang B-M, Wang D-F, Wu Z-J. Effects of cure cycles on void content and mechanical properties of composite laminates. Compos Struct Jun. 2006;73(3): 303–9. https://doi.org/10.1016/j.compstruct.2005.02.001.
- [4] Lambert J, Chambers AR, Sinclair I, Spearing SM. 3D damage characterisation and the role of voids in the fatigue of wind turbine blade materials. Compos Sci Technol Jan. 2012;72(2):337–43. https://doi.org/10.1016/j.compscitech.2011.11.023.
- [5] Di Landro L, Montalto A, Bettini P, Guerra S, Montagnoli F, Rigamonti M. Detection of Voids in Carbon/Epoxy Laminates and Their Influence on Mechanical Properties. Polym Polym Compos Jun. 2017;25(5):371–80. https://doi.org/10.1177/ 096739111702500506.
- [6] Sisodia SM, Bull DJ, George AR, Gamstedt EK, Mavrogordato MN, Fullwood DT, et al. The effects of voids in quasi-static indentation of resin-infused reinforced polymers. J Compos Mater 2019;53(28-30):4399–410.
- [7] Mehdikhani M, Gorbatikh L, Verpoest I, Lomov SV. Voids in fiber-reinforced polymer composites: A review on their formation, characteristics, and effects on

- mechanical performance. J Compos Mater May 2019;53(12):1579–669. https://doi.org/10.1177/0021998318772152.
- [8] Schell JSU, Deleglise M, Binetruy C, Krawczak P, Ermanni P. Numerical prediction and experimental characterisation of meso-scale-voids in liquid composite moulding. Compos A Appl Sci Manuf Dec. 2007;38(12):2460–70. https://doi.org/ 10.1016/j.compositesa.2007.08.005.
- [9] Hamidi YK, Aktas L, Altan MC. Effect of packing on void morphology in resin transfer molded E-glass/epoxy composites. Polym Compos 2005;26(5):614–27. https://doi.org/10.1002/pc.20132.
- [10] S. Hernández, F. Sket, C. González, and J. LLorca, "Optimization of curing cycle in carbon fiber-reinforced laminates: Void distribution and mechanical properties," *Composites Science and Technology*, vol. 85, pp. 73–82, Aug. 2013, doi: 10.1016/j. compscitech.2013.06.005.
- [11] H. Teixidó, J. Staal, B. Caglar, and V. Michaud, "Capillary Effects in Fiber Reinforced Polymer Composite Processing: A Review," Frontiers in Materials, vol. 9, 2022, Accessed: Nov. 28, 2022. [Online]. Available: https://www.frontiersin.org/ articles/10.3389/fmats.2022.809226.
- [12] Kim YR, McCarthy SP, Fanucci JP. Compressibility and relaxation of fiber reinforcements during composite processing. Polym Compos 1991;12(1):13–9. https://doi.org/10.1002/pc.750120104.
- [13] Robitaille F, Gauvin R. Compaction of textile reinforcements for composites manufacturing. III: Reorganization of the fiber network. Polym Compos 1999;20 (1):48–61. https://doi.org/10.1002/pc.10334.
- [14] Grieser T, Mitschang P. Investigation of the compaction behavior of carbon fiber NCF for continuous preforming processes. Polym Compos 2017;38(11):2609–25. https://doi.org/10.1002/pc.23854.
- [15] Lectez A-S, El Azzouzi K, Binetruy C, Comas-Cardona S, Verron E, Lebrun J-M. Three-dimensional mechanical properties of dry carbon fiber tows subjected to cyclic compressive loading. J Compos Mater Aug. 2018;52(19):2661–77. https://doi.org/10.1177/0021998317752229.
- [16] Pearce N, Summerscales J. The compressibility of a reinforcement fabric. Compos Manuf Jan. 1995;6(1):15–21. https://doi.org/10.1016/0956-7143(95)93709-8.
- [17] Niggemann C, Song YS, Gillespie JW, Heider D. Experimental Investigation of the Controlled Atmospheric Pressure Resin Infusion (CAPRI) Process. J Compos Mater Jun. 2008;42(11):1049–61. https://doi.org/10.1177/0021998308090650.
- [18] Somashekar AA, Bickerton S, Bhattacharyya D. Exploring the non-elastic compression deformation of dry glass fibre reinforcements. Compos Sci Technol Feb. 2007;67(2):183–200. https://doi.org/10.1016/j.compscitech.2006.07.032.
- [19] George A, Hannibal P, Morgan M, Hoagland D, Stapleton SE. Compressibility measurement of composite reinforcements for flow simulation of vacuum infusion. Polym Compos 2019;40(3):961–73. https://doi.org/10.1002/pc.24770.
- [20] Danzi M, Klunker F, Ermanni P. Experimental validation of through-thickness resin flow model in the consolidation of saturated porous media. J Compos Mater Jul. 2017;51(17):2467–75. https://doi.org/10.1177/0021998316671574.
- [21] Yenilmez B, Caglar B, Sozer EM. Viscoelastic modeling of fiber preform compaction in vacuum infusion process. J Compos Mater Dec. 2017;51(30):4189–203. https://doi.org/10.1177/0021998317699983.
- [22] Yenilmez B, Caglar B, Sozer EM. Pressure-controlled compaction characterization of fiber preforms suitable for viscoelastic modeling in the vacuum infusion process. J Compos Mater Apr. 2017;51(9):1209–24. https://doi.org/10.1177/ 0021998316685164
- [23] Matsuzaki R, Seto D, Todoroki A, Mizutani Y. Void formation in geometry-anisotropic woven fabrics in resin transfer molding. Adv Compos Mater Mar. 2014;23(2):99–114. https://doi.org/10.1080/09243046.2013.832829.
- [24] Lundström TS, Gebart BR. Influence from process parameters on void formation in resin transfer molding. Polym Compos 1994;15(1):25–33. https://doi.org/ 10.1002/pc.750150105.
- [25] Castro J, Sket F, Helfen L, González C. In situ local imaging and analysis of impregnation during liquid moulding of composite materials using synchrotron radiation computed laminography. Compos Sci Technol Oct. 2021;215:108999. https://doi.org/10.1016/j.compscitech.2021.108999.
- [26] Patel N, Lee LJ. Effects of fiber mat architecture on void formation and removal in liquid composite molding. Polym Compos 1995;16(5):386–99. https://doi.org/ 10.1002/pc.750160507.
- [27] Park CH, Woo L. Modeling void formation and unsaturated flow in liquid composite molding processes: a survey and review. J Reinf Plast Compos Jun. 2011;30(11):957–77. https://doi.org/10.1177/0731684411411338.
- [28] Staffan Lundström T, Frishfelds V, Jakovics A. Bubble formation and motion in non-crimp fabrics with perturbed bundle geometry. Compos A Appl Sci Manuf Jan. 2010;41(1):83–92. https://doi.org/10.1016/j.compositesa.2009.05.012.
- [29] Fast T, Scott AE, Bale HA, Cox BN. Topological and Euclidean metrics reveal spatially nonuniform structure in the entanglement of stochastic fiber bundles. J Mater Sci Mar. 2015;50(6):2370–98. https://doi.org/10.1007/s10853-014-8766-2
- [30] Czabaj MW, Riccio ML, Whitacre WW. Numerical reconstruction of graphite/epoxy composite microstructure based on sub-micron resolution X-ray computed tomography. Compos Sci Technol Dec. 2014;105:174–82. https://doi.org/ 10.1016/j.compscitech.2014.10.017.
- [31] Creveling PJ, Whitacre WW, Czabaj MW. A fiber-segmentation algorithm for composites imaged using X-ray microtomography: Development and validation. Compos A Appl Sci Manuf Nov. 2019;126:105606. https://doi.org/10.1016/j. compositesa.2019.105606.
- [32] Weissenböck J, Bhattacharya A, Plank B, Heinzl C, Kastner J. Visual classification of braided and woven fiber bundles in X-ray computed tomography scanned carbon fiber reinforced polymer specimens. Case Stud NondestrTest Eval Nov. 2016;6: 39-46. https://doi.org/10.1016/j.csndt.2016.05.006.

- [33] Sencu RM, Yang Z, Wang YC, Withers PJ, Rau C, Parson A, et al. Generation of micro-scale finite element models from synchrotron X-ray CT images for multidirectional carbon fibre reinforced composites. Compos A Appl Sci Manuf 2016;91:85–95
- [34] Scott AE, Sinclair I, Spearing SM, Thionnet A, Bunsell AR. Damage accumulation in a carbon/epoxy composite: Comparison between a multiscale model and computed tomography experimental results. Compos A Appl Sci Manuf Sep. 2012;43(9): 1514–22. https://doi.org/10.1016/j.compositesa.2012.03.011.
- [35] Nguyen NQ, Mehdikhani M, Straumit I, Gorbatikh L, Lessard L, Lomov SV. Micro-CT measurement of fibre misalignment: Application to carbon/epoxy laminates manufactured in autoclave and by vacuum assisted resin transfer moulding. Compos A Appl Sci Manuf Jan. 2018;104:14–23. https://doi.org/10.1016/j.compositesa.2017.10.018.
- [36] Sanei SHR, Barsotti EJ, Leonhardt D, Fertig RS. Characterization, synthetic generation, and statistical equivalence of composite microstructures. J Compos Mater 2017;51(13):1817–29.
- [37] Wang L, Nygren G, Karkkainen RL, Yang Q. A multiscale approach for virtual testing of highly aligned short carbon fiber composites. Compos Struct Dec. 2019; 230:111462. https://doi.org/10.1016/j.compstruct.2019.111462.
- [38] "Robo-Met Materials Characterization | UES, Inc." https://www.ues.com/robomet (accessed Nov. 24, 2021).
- [39] Schneider CA, Rasband WS, Eliceiri KW. NIH Image to ImageJ: 25 years of image analysis. Nat Methods Jul. 2012;9(7):671–5. https://doi.org/10.1038/ nmeth.2089.
- [40] Schey MJ, Beke T, Appel L, Zabler S, Shah S, Hu J, et al. Identification and Quantification of 3D Fiber Clusters in Fiber-Reinforced Composite Materials. JOM 2021;73(7):2129–42.